LANGMUIR

pubs.acs.org/Langmuir Article

Concentration Dependence of a Hydrogel Phase Formed by the Deprotonation of the Imidazole Side Chain of Glycylhistidylglycine

Morgan Hesser, Lavenia J. Thursch, Todd R. Lewis, Thamires A. Lima, Nicolas J. Alvarez,* and Reinhard Schweitzer-Stenner*

Cite This: *Langmuir* 2021, 37, 6935−6946 Read Online

ACCESS | Metrics & More | Article Recommendations | Supporting Information

ABSTRACT: Upon deprotonation of its imidazole group at ∼pH 6, the unblocked tripeptide glycylhistidylglycine (GHG) self-assembles into very long crystalline fibrils on a 10−1000 μm scale which are capable of forming a volume spanning network, that is, hydrogel. The critical peptide concentration for self-assembly at a pH of 6 lies between 50 and 60 mM. The fraction of peptides that self-assemble into fibrils depends on the concentration of deprotonated GHG. While IR spectra seem to indicate the formation of fibrils with standard amyloid fibril β-sheet structures, vibrational circular dichroism spectra show a strongly enhanced amide I′ signal, suggesting that the formed fibrils exhibit significant chirality. The fibril chirality appears to be a function of peptide concentration. Rheological measurements reveal that the rate of gelation is concentration-dependent and that there is an optimum gel strength at intermediate peptide concentrations of ca. 175 mM. This paper outlines the unique properties of the GHG gel phase which is underlain by a surprisingly dense fibril network with an exceptionally strong modulus that make them potential additives for biomedical applications.

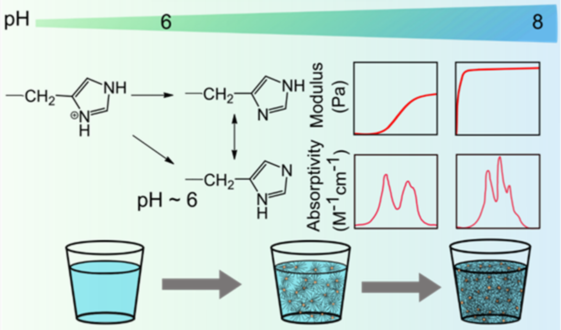

■ INTRODUCTION

Over the last 15−20 years, a plethora of papers and review articles have appeared which reported the self-assembly of mid-sized to short oligopeptides into supramolecular structures such as nanotubes and scaffold-forming hydrogels.[1−7] The latter is potentially relevant for biotechnological purposes such as drug release and tissue repair. For a long period of time, it was thought that the number of residues in an oligopeptide has to exceed a certain threshold (m = 10−12) to self-assemble into ordered fibrils.[8,9] However, short peptides (m < 10) with strong aromatic components have been shown to be quite capable of forming supramolecular structures on the nanometer and micron scales, including very stable hydrogels or gels in mixtures of dimethylsulfoxide (DMSO) and water.[3,10−13] A canonical example is the dipeptide fluorenylmethyloxycarbonyl-di-phenylalanine and its derivatives (FmocFF).[14−16] The respective fibrils are formed by the self-assembly of β-sheets via π−π stacking between phenylalanine residues.[17−19] This discovery prompted computational studies which suggested that aromaticity is pivotal for the propensity of short oligopeptides to self-assemble.[20,21]

Recently, our research groups discovered a new class of rather unexpected gelators that form supramolecular structures that are quite different from those observed with short aromatic oligopeptides.[22,23] Hydrogel phases formed with the latter are generally underlain by a network of rather thin fibrils with an axial dimension of 10^{-8}−10^{-6} m. (Note that the term hydrogel is used even if the solvent is a binary mixture of water).[24] We observed hydrogel phases formed by two unblocked tripeptides, namely, glycylalanylglycine (GAG)[24] and glycylhistidylglycine (GHG),[25] the former in water−ethanol mixtures and the latter in water via deprotonation of the imidazole side chain. Several observations have been made regarding the propensity of these peptides to self-assemble. For example, GAG must be in its cationic state and above a critical concentration to form a gel. The critical concentration depends on the ethanol fraction and was found to vary between ca. 60 mM for high ethanol mole fractions (0.8) and 350 mM for ethanol mole fractions around 0.35.[26,27] The gelation of GHG seems to require the deprotonation of the imidazole ring occurring at pH >6 and a concentration above ∼50 mM, but a more precise determination of critical conditions for self-assembly and gelation is still outstanding.

While GAG gels have already been investigated extensively,[24,26−28] our understanding of GHG gelation is yet in its

Received: February 9, 2021
Revised: May 18, 2021
Published: June 2, 2021

ACS Publications

https://doi.org/10.1021/acs.langmuir.1c00382

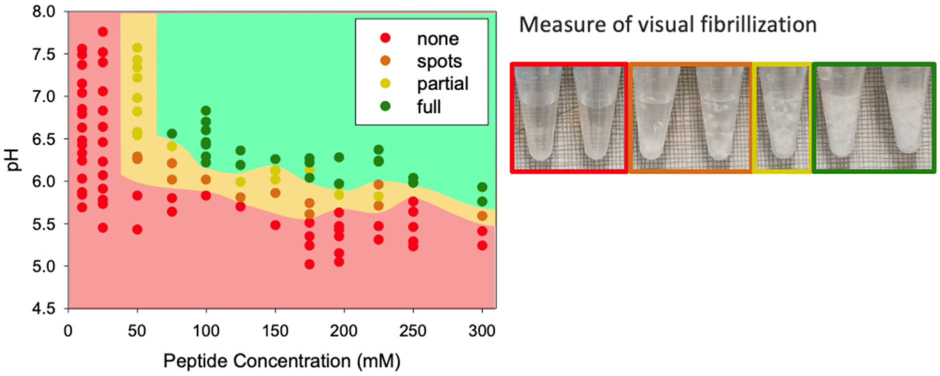

Figure 1. Left: Phase diagram of GHG in water with respect to peptide concentration and solution pH. Samples were characterized visually as those showing no visible large-scale peptide aggregates (red dots in red phase), those with partial aggregation (yellow and orange dots in yellow phase), and nearly complete aggregation (dark green dots in light green phase). The background has been added as a visual guide for the identification of phases. Right: GHG samples illustrating the visibility of large-scale aggregates indicated by the dots in the phase diagram.

infancy.[25] Even though imidazole is aromatic in the deprotonated state, it is by no means a top candidate for promoting large-scale self-assembly.[21] However, what distinguishes imidazole from other amino acid side chains is its avidity for hydrogen bonding. At neutral pH, the equilibrium between the π-tautomer (NεH) and the τ-tautomer (NδH) is dominated by the former in the zwitterionic state of the peptide.[29] The π-tautomer has been shown to act as a hydrogen bonding donor and acceptor, whereas the τ-tautomer frequently involves hydrogen bonding with amide protons of protein backbones.[30] Apparently, this capability is diminished in the protonated state of the imidazole ring where it can function solely as a hydrogen-bonding donor. The relevance of the histidine's protonation state for the self-assembly of peptides has been emphasized earlier. Nanofibril formation by the oligopeptide H6 occurs between pH 5 and 6.5, which is clearly indicative of imidazole deprotonation as the facilitator.[31] The fibrillization and gelation of an octa-peptide that contained only a single histidine residue at the C-terminal was found to require a nearly neutral pH.[32] Together with our own observations, these results suggest that deprotonated histidine is a strong promoter of self-assembly into fibrils.

Figure 1 shows an earlier reported two-dimensional phase diagram for GHG in water, illustrating a critical pH for fibrillization that decreases with increasing peptide concentration.[25] It suggests that above pH 6.2, the self-assembly of GHG requires a dissolved peptide concentration of ca. 50 mM. The critical pH varies between ca. 6.2 at 50 mM and ca. 5.8 at submolar peptide concentration. IR and vibrational circular dichroism (VCD) spectra obtained for a gel formed in a sample of 175 mM GHG at pH 6.39 seemed to suggest that GHG forms a sol−gel mixture of helically twisted β-sheet and soluble monomers/amorphous aggregates that are not incorporated in the gel,[25] but this interpretation requires further validation. Rheological data measured with the same sample revealed a strong gel with a storage modulus between 40 and 50 kPa and tan δ values between 0.1 and 0.2.[25]

Several important questions remain regarding the nature of GHG self-assembly via pH switching. For example, it is unclear to what extent the decrease in critical pH reflects a decrease in the effective pK value that results from the stabilization of the deprotonated state by self-assembly and gelation. Moreover, it is yet unknown how the formation of sheets and fibrils under different conditions (i.e., pH and peptide concentration) affects the network macrostructure and gel strength. While the storage moduli of peptide gels generally exhibit a monotonic function of the peptide concentration,[33,34] the gel strength for GAG gels in the water/ethanol mixture was found to reach a maximum at peptide concentration between 200 and 250 mM peptide concentration in the mixture of 55 mol % ethanol and 45 mol % water.[28] Finally, it is unclear whether the sheet structure that underlies the observed crystalline fibrils is a typical β-sheet. This cannot be taken for granted in view of our earlier findings of a non β-sheet structure for GAG fibril networks.[24,27,35]

This paper aims to address these issues via rheological, IR/vibrational circular dichroism (VCD) and conventional microscopy measurements of three different peptide concentrations (75, 175, and 300 mM) at different pH values. These concentrations are positioned at the corners and the center of the phase diagram reported by Hesser et al.[25] Our results reveal an intricate relationship between the fibril structure, gel strength, fibrillization network, and peptide concentration.

■ MATERIALS AND METHODS

Materials. L-Glycyl-L-histidyl-L-glycine (GHG) acetate salt was obtained from Bachem Biosciences Inc. (King of Prussia, PA) with >99% purity and used without further purification. The absence of trifluoroacetic acid (TFA) was confirmed by IR spectroscopy. Deuterated water (D_2O) was the solvent used (99.9% purity, Aldrich and 99.8% purity, TCI). The pD was adjusted using deuterium chloride (DCl) (35 wt % in D_2O, 99 atom % D, Aldrich) and sodium deuteroxide (NaOD) (30 wt % in D_2O, 99 atom % D, Aldrich).

Sample Preparation. Since all the IR and VCD experiments had to be performed in D_2O, DCl and NaOD were used for adjusting the pD of the sample. Generally, a value of 0.4 has to be added to the measured pH value to calculate the corresponding pD.[36] However, for practical purposes outlined below, we report the measured pH value and denote it as pH*. A stock solution of GHG (ca. 400 mM) was prepared in acidic D_2O. To dissolve the peptide, the pH* was adjusted by the addition of DCl until no solid peptide sample was observed. This was vortexed and allowed to sit ca. 10 min to ensure complete dissolution. Dissolution was confirmed visually, as the suspended peptide particles are opaque white, while the dissolved peptide is clear and colorless. The final pH* as measured at ambient temperature was between 2 and 3 for all samples. The final concentration of this stock solution was ca. 400 mM. Information about the amount of GHG used to produce the stock solutions and their concentrations and pH* values is listed in Table S1.

The peptide samples investigated in this study were prepared from the stock solution listed in Table S1. First, we determined the necessary amount of stock solution to obtain a final sample volume of

https://doi.org/10.1021/acs.langmuir.1c00382

ca. 400 μL. Next, an aliquot of stock solution of the proper volume was pipetted into an Eppendorf tube. The final volume of the sample was prepared by adding an appropriate combination of D_2O and NaOD. D_2O was added to the stock solution in the Eppendorf tube, and the resulting solution was vortexed to mix. This solution was kept at 25 °C in a water bath for a minimum of 10 min prior to the addition of a base. The base solution was also equilibrated for the same time in the same bath. For the preparation of the 300 mM, pH* 6.61 sample, a 1:5 dilution of stock NaOD in D_2O was used. For all other samples, we employed a 1:10 dilution of the stock NaOD in D_2O. The exact volumes used to make each solution are given in Table S2.

To prepare the different gel samples, the dilute NaOD solution was pipetted into the stock peptide and D_2O solution. The thus-prepared sample was vortexed again briefly (ca. 5 s). The pH* was measured prior to the appearance of light-scattering aggregates by a properly calibrated Fisher Scientific Accument AR50 pH probe, software revision 1.04b. The sample was then prepared for use depending on the utilized experimental technique. For spectroscopy measurements, the sample was pipetted into the appropriate cell (discussed below) to allow for gel formation. For rheological measurements, the sample was transferred to the rheometer plates. For microscopy, it was mounted using a pipette onto a slide. In all cases, the sample was transferred prior to the formation of visible aggregates.

All experiments were carried out under temperature-controlled conditions at 25 °C. For steady-state experiments, including the measurement of gel spectra, samples were left for a minimum of 2 h before commencing the measurement to ensure complete gelation (cf. the below-reported and discussed gelation kinetics). For kinetic measurements, the start (t = 0 s) was recorded as the time when the base solution was added to the sample.

Infrared and VCD Spectroscopy. All infrared spectroscopy experiments were performed with peptides in deuterated water. For IR measurements performed as a function of peptide concentration pH*, samples were loaded into a CaF_2 biocell from BioTools with pathlengths of 15 or 122 μm. The specific pathlength for each measurement was used to convert the measured absorbance to molar absorptivity. Sample temperature was maintained using a BioTools water-cooled temperature controller. This was set to 25 °C to agree with rheological measurements of the corresponding samples.

Fourier transform infrared (FTIR) spectra were measured on a BioTools ChiralIR. Spectra taken in conjunction with VCD measurements were collected with a resolution of 8 cm^{-1} and scan speed of 83 scans per minute using Grams/IR 7.00 software (Thermo Galactic). IR spectra taken without a concurrent VCD measurement were collected with a resolution of 8 cm^{-1} as the average of 350 scans. IR spectra were not solvent-corrected, as doing so resulted in negative absorbance values. This observation indicates that gelation changes the spectrum of water by encapsulation into the gel structure.

Part of the observed IR spectra in the region from 1400 to 1800 cm^{-1} were decomposed into individual Gaussian bands in the amide I′ region and Voigtian bands (COO^{-}_{as}) using MULTIFIT software[37] and an in-house spectral decomposition program written in Matlab. The Matlab decomposition also accounted for a Voigtian character in the lowest-wavenumber amide I′ band. The MULTIFIT fitting routine has an internal check to determine when the fit is satisfactory. Both fitting routines utilized least-squares procedures.

In order to check for birefringence, the sample cell was rotated ca. 120° and spectra were retaken, resulting in three total spectra at three different orientations. The sample cell was marked so that the alignment was reproducible for later experiments. Measurements of the pure solvent (not shown) indicated no apparent artifacts.

For VCD experiments, samples were prepared in the same way as for FTIR, utilizing the same Chiral IR spectrometer. Solution spectra were taken for 10 h in order to gain an appropriate signal-to-noise ratio. Gel spectra were collected for 1 h, as the enhanced signal in the amide I′ region was sufficiently distinguishable after that time.

In addition to IR spectra measured with the abovementioned BioTools instrument, we used the ATR setup of a Thermo Nicolet Nexus 870 FT-IR spectrometer in the absorbance mode to record the kinetics of peptide self-assembly at 175 mM. The spectra were recorded with 32 scans at a 4 cm^{-1} resolution at room temperature with a deuterated triglycine sulfate (DTGS) detector in the 650−4000 cm^{-1} range for mid-infrared (M-IR) spectra. The kinetics experiments were performed every minute for 30 min starting right after gel formation.

Rheology. Rheology measurements were obtained using the abovementioned solutions. Measurements were taken using a DHR-3 (TA Instruments) using a Peltier temperature-controlled plate maintaining a constant temperature of 25 °C. The top plate diameter was 25 mm. A gap of 700 μm was used for all steps. Mechanical properties were probed using small-amplitude oscillatory shear measurements. Angular frequency sweeps were made from 100 to 10^{-3} rad s^{-1} using a 0.03% strain.

To avoid solvent evaporation, safflower oil was added as a solvent trap around the free surface of the sample. The samples were prepared 1−3 min prior to loading. Note that t = 0 was recorded when the base was added to the solubilized peptide solution.

Microscopy. Microscopy images of GHG gels were taken of the same samples used for rheological experiments. The freshly prepared peptide solutions were pipetted into concave microscope slides in triplicates. Images were taken after 200 min or at the time when the storage modulus plateaued, as determined by rheology. The microscopic images were acquired using an Amscope 7X-45X Trinocular Stereo Zoom brightfield microscope equipped with an Amscope MU130 camera.

■ RESULTS AND DISCUSSION

This section of the paper is organized as follows. In the first step, we use the phase diagram reported by Hesser et al.[25] (Figure 1) to estimate the concentration of deprotonated histidine at the boundary between the gel and sol phase. Next, we report and analyze the IR and VCD spectra of the gel phase at different peptide concentrations and pH*. The kinetics of GAG self-assembly is probed by time-dependent IR spectroscopy. Subsequently, we examine kinetics and strength of the gel phase. Finally, we turn to microscopy to probe how the formed sample-spanning network depends on peptide concentration. It should be noted that in the following, we use the term "deprotonated GHG" for the zwitterionic state of the peptide.

Relationship between pK_a and Critical pH for Self-Assembly. Figure 1 shows that the critical pH decreases from ca. 6.4 to 5.8 with increasing peptide concentration, which suggests that self-assembly occurs at pH values above the pK value of the imidazole side chain.[25] We wondered whether similar critical concentrations of deprotonated GHG could be obtained for the three peptide concentrations investigated. To check for this possibility, we calculated the concentration of deprotonated peptides as a function of pH using

$$[\mathrm{GHG}]_{\mathrm{deprot}} = \frac{[\mathrm{GHG}]_0}{K_a[\mathrm{H_3O^+}] + 1} \tag{1}$$

where $[\mathrm{GHG}]_0$ is the initial peptide concentration, K_a denotes the equilibrium constant of imidazole protonation, and $[\mathrm{H_3O^+}]$ is the hydronium ion concentration. Equation 1 can be easily derived from the respective mass action law and mass conservation. For GHG monomers, K_a would correspond to a pK value of 6.48.[25] We used eq 1 to calculate the titration curves for the three peptide concentrations which are shown in Figure S1 together with the $[\mathrm{GHG}]_{\mathrm{deprot}}$ values calculated for the corresponding critical pH values of the boundaries between the red and yellow and between the yellow and green phase, which are indicated by yellow diamonds and green circles, respectively. The corresponding values lie in narrow regions between 0.03 and 0.04 mM for the red-yellow and between 0.035 and 0.045 mM for the yellow-green boundary, suggesting that the critical concentrations of deprotonated GHG are very similar for the three investigated total peptide concentrations.

If the underlying self-assembly of peptides is a highly cooperative process, it can be represented by a very simple scheme

$$\mathrm{GHG_{deprot}} + [\mathrm{H_3O^+}] \rightleftharpoons \mathrm{GHG_{prof}} \qquad (2)$$

$$n\mathrm{GHG_d} \rightleftharpoons (\mathrm{GHG_d})_n$$

While the obtained similarities of critical peptide concentrations meet expectations, the use of the solution pK_a of 6.48[25] seems to be counterintuitive. One would expect that fibrillization and gelation should stabilize the deprotonated state and thus give rise to a lower apparent pK value. We therefore used eq 1 to calculate the titration curves for lower pK_a values and found that even a small decrease in the latter significantly increases the difference between the critical concentrations for the two-phase boundaries.

We wondered whether this issue could be resolved by considering the different ionic strengths of the highly concentrated peptide solutions used in the current study and the 10 mM solution employed for the determination of the pK value of the GHG monomer. As described in Material and Methods, GHG was first titrated into the acidic region (all groups protonated) by adding DCl to ensure sufficient solubility. Subsequently, NaOD was added to achieve the indicated pH*(pD) value. Moreover, the as-received solid GHG sample is an acetate salt which produces an acidic pH*(pD) upon dissolution in aqueous solution. This protocol produces concentrations of sodium, chloride, and acetate ions which together amount to approximately twice the peptide concentration, since two groups (COO^- and imidazole) are first protonated by the involved acids and subsequently deprotonated by NaOD. Therefore, the apparent pK of the imidazole side chain must take into account the influence of the employed ionic strength of the sample using the Debye–Hückel correction[38]

$$pK_a = pk_0 + \frac{3A\sqrt{I}}{1 + B\sqrt{I}} \qquad (3)$$

where $A = 0.51\ \mathrm{M}^{-1/2}$ and $B = 1.6\ \mathrm{M}^{-1/2}$. The ionic strength I was estimated in molar units. pk_0 is the pK value of solution at zero ionic strength. We varied the pK_0 value until we minimized the difference between the respective critical $[\mathrm{GHG}]_{\mathrm{deprot}}$ values for the three peptide concentrations investigated. Thus, we obtained a pK_0 value of 6.0. The updated values of $[\mathrm{GHG}]_{\mathrm{deprot}}$ between the red and yellow boundaries (yellow diamonds) and yellow and green boundaries (green circles) are between 0.028 and 0.039 mM and 0.043 and 0.052 mM, respectively. Note that these values are very similar to those inferred from the titration curves calculated with eq 1. In view of the uncertainties of the boundaries in Figure 1, we consider the precision of our estimation of critical concentrations for fibril formation and gelation as sufficient. The fact that the pK_0 value now differs from the expected pK_a value of 6.48 suggests that self-assembly stabilizes the deprotonated state by a Gibbs free energy of approximately 18 kJ/mol. However, the high ionic strength of the samples used for the self-assembly experiments causes the effective pK_a to be practically identical to the monomeric value.

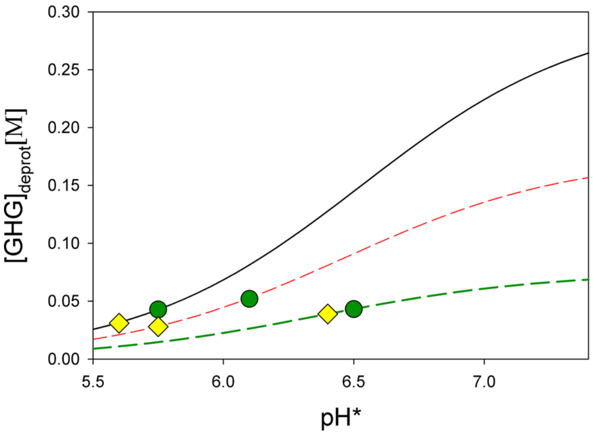

Figure 2. Concentration of deprotonated GHG calculated as a function of pH by means of eq 1 for 75 mM (green short dash), 175 mM (red long dash), and 300 mM (black line) total GHG concentration. The earlier reported a pK value of 6.48 was used for the calculation.[25] The samples forming at the full aggregation boundary between the yellow and green phase of the phase diagram in Figure 1 are indicated by yellow diamonds (highest pH* without full aggregation at a given concentration) and green circles (lowest pH with full aggregation at a given concentration).

In what follows, we will use the titration curves visualized in Figure 2 to relate the concentration of deprotonated GHG to the change in amide I′ profiles. Figure S2 shows the same titration curves as Figure 2 but with black dots indicating the GHG concentrations used for our spectroscopic and rheological experiments. The concentrations of deprotonated GHG at the critical pH* of the red-yellow and yellow-green boundaries indicated by yellow diamonds and green circles lie between 0.043 and 0.052 mM for the red-yellow boundary and between 0.028 and 0.039 mM for the yellow-green boundary. In view of the uncertainties of the boundaries in Figure 1, we consider the precision of our estimation of critical concentrations for fibril formation and gelation as sufficient.

Analysis of FTIR Spectra Taken at Different Points of the Gel Phase. Figure 3 shows the IR spectra of self-assembled fibrils between 1500 and 1750 cm^{-1} formed with 75, 175, and 300 mM GHG in D_2O for different pH* values. Note that all points are representative of self-assembled fibrils forming a hydrogel, as confirmed by rheology (*vide infra*). The pH* values are reported as displayed by the pH probe and have not been corrected to pD values which are generally ca. 0.4 units higher than the measured value. This allowed us to relate our spectroscopic data to the phase diagram in Figure 1 and the calculation in the preceding paragraph. We argue that such data representation is permissible because pK values of protonable groups shift up by nearly the same amount in D_2O.[36]

Before discussing the results, we first acknowledge that given the length of GHG fibrils and their propensity to form bundles, the fibril networks might result in anisotropic macrostructures. Note that anisotropic networks were reported for the gel phases of cationic GAG.[26] Anisotropy is known to cause birefringence effects that influence recorded VCD and IR spectra.[40,41] While newer instruments are capable of correcting birefringence effects, the spectrometer model used in this study does not fully eliminate them. Thus, to probe for the influence of birefringence on the recorded spectra, we recorded the

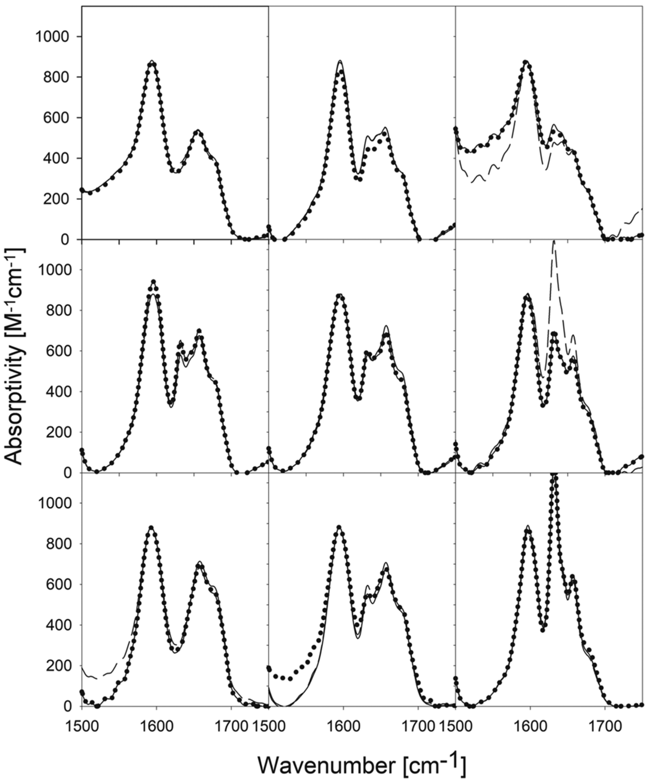

Figure 3. IR spectra of 75 (upper panel), 175 mM (middle panel), and 300 mM GHG (lower panel) at pH* 6.67, 6.33, and 5.70 (left), 6.97, 6.47, and 5.92 (middle), and 7.38, 6.84, and 6.13 (right) in the region between 1500 and 1750 cm^{-1}. The sample was rotated approximately 120° between scans, with the corresponding spectra labeled R1 (solid line), R2 (dashed), and R3 (dot). All spectra were normalized on the COO$^{-}_{as}$ band at 1596 cm^{-1} for which we assumed a peak molar absorptivity of 880 M^{-1} cm^{-1}.[39]

spectra for three different orientations of the sample termed R1, R2, and R3, which differ by ca. 1200. Figure S3 shows that the spectra depend rather significantly on the rotation angle of the biocell. Fortunately, upon closer inspection, we observe that most of the differences are quantitative rather than qualitative and thus could be eliminated by normalizing all spectra on the COO^{-} antisymmetric stretching (COO$_{as}$) band at 1595 cm^{-1} as measured with R1 orientation with the 75 mM GHG sample at pH* 6.67. The corresponding peak molar absorptivity of this band (880 M^{-1} cm^{-1}) is close to experimental values of this band in tripeptide monomers.[39] The normalized spectra are shown in Figure 3. While the quantitative differences between the measured spectra documented by Figure S3 reflect inhomogeneous densities of peptides in the sample caused by the self-assembly of peptide fibrils, the qualitative differences observed for 175 mM spectra measured at pH* 6.84 most likely reflect an anisotropic character of the gel phase.

All bands between 1600 and 1700 cm^{-1} are assignable to amide I′. All spectral series show the same trend regarding changes in the amide I′ band profile. At the lowest pH*, the spectra resemble the doublet seen in the sol phase spectrum. It is indicative of a mixture of extended conformations (polyproline II and β-strand).[23] With increasing pH*, a peak in the 1630 cm^{-1} region appears and increases with pH* and also with peptide concentration. The appearance of this band in the IR spectrum of the gel phase formed with 175 mM GHG has been reported earlier by Hesser et al. and assigned to β-sheets, in accordance with the current literature.[25] However, we will offer a somewhat modified view based on our spectral analysis described below. Irrespective of any structural interpretation, we conclude that the band at 1630 cm^{-1} is an indicator for the formation of long-scale self-assembled fibrils that precede the formation of physically cross-linked fibrils in the gel network. As expected, our data seem to indicate that the number of fibrils in the gel network increased with pH* and peptide concentration, which both produce higher concentrations of deprotonated peptides (vide infra).

Figure 3 clearly shows that the amide I′ region peaks are observed at the same wavenumbers for all three samples, which indicates that the underlying structures are the same. One interesting difference is the unique feature observed for the 300 mM sample; namely, the pH-dependent band at 1632 cm^{-1}, which exceeds the COO-antisymmetric stretch intensity at pH* 6.13. We analyzed the spectroscopic data using an in-house MatLab program for spectral decomposition (cf. Material and Methods). The influence of bands below 1500 cm^{-1} on the spectral analysis of the COO$^{-}_{as}$/amide I′ region was accounted for by performing the spectral decomposition over the entire region between 1300 and 1800 cm^{-1}. Figure S4 shows examples of the resultant spectral decomposition. Our analysis yielded four amide I′ bands at ca. 1632 (AI$_1$), 1644 (AI$_2$), 1657 (AI$_3$), and 1678 cm^{-1}(AI$_4$) (Figure S4). Their wavenumbers were found to vary within intervals of 2 cm^{-1} for

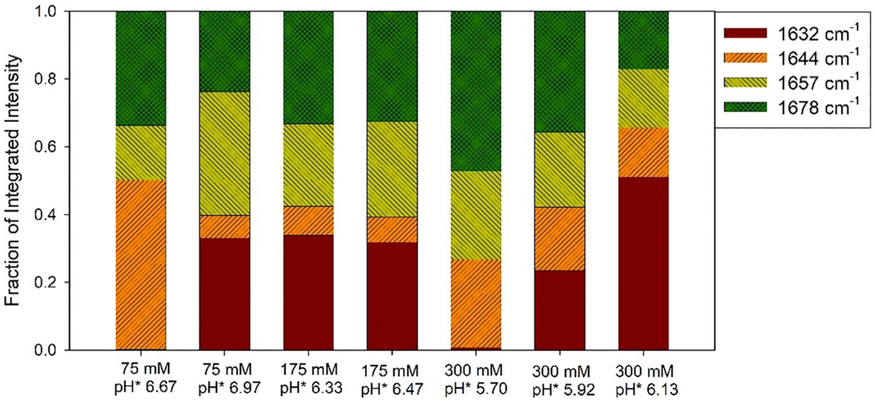

Figure 4. Fractional intensities of sub bands in the amide I′ region of GHG in D$_2$O obtained from the spectral decomposition of spectra measured with the indicated peptide concentration and pH*.

AL_1, AI_3 and AI_4 and of 4 cm^{-1} for AI_2. Respective bandwidths were found to depend on the orientation of the cell. We calculated the fractional intensities of these bands by normalizing their integrated intensities on the total intensity of the amide I′ band profile. The analysis was performed for spectra taken with different sample orientations (Figures 3 and S3). The average fractional intensities of the abovementioned amide I′ sub bands are depicted in Figure 4.

Based on their respective wavenumbers, the assignment of these four bands seems to be straightforward. For example, AI_3 and AI_4 are very close to the positions of the two amide I′ bands of GHG in solution,[23] while AI_1 and AI_2 are both in a region where one expects contributions from β-sheets.[42−45] Different wavenumbers of the latter can be indicative of different sheet lengths or different degrees of deformation by, for example, twisting.[44,46] If the spectra reflected a mixture of dissolved monomers and gel-integrated fibrils, one would expect a two-state behavior (monomer fibril) with the two high-wavenumber band intensities (monomer) decreasing and the two low-wavenumber band intensities (fibrils) synchronously increasing with higher peptide concentration and pH*. However, such a behavior was only observed for the 300 mM samples. Figure 4 shows that for the 300 mM samples, the combined intensity of AI_1 and AI_2 increases with increasing pH*, while the combined intensity of AI_3 and AI_4 decreases. In order to check whether the intensity distribution would change further in favor of AI_1 and AI_2, we measured the IR spectrum of a gel created at pH* 6.61 (80 mM deprotonated GHG). The spectrum is shown in Figure S5. It very much resembles the pH* 6.13 spectrum and exhibits only a slight increase in AI_1 (Figure 4). While the trends exhibited by the two groups of bands seem to support a two-state scenario, one has to note that the variations of the relative intensities within these two groups are at variance with a simple two-state model. In the lower-wavenumber group, the intensity gain of AI_1 with increasing pH* occurs in part at the expense of AI_2, which indicates an increasing population of more ordered fibrils. The high-wavenumber group is dominated by AI_4 at low pH*, while both bands depict similar intensities at high pH*. Overall, the intensity of AI_3 decreases only slightly with pH*, while the intensity of AI_4 decreases significantly. This observation implies that the overall loss of intensity of the high wavenumber group occurs mostly at the expense of AI_4. Interestingly, only the $\mathrm{AI}_3/\mathrm{AI}_4$ intensity ratio observed at high pH* actually resembles the intensity ratio of the two amide I′ bands in the spectrum of GHG monomers, which is indicative of a dominance of extended polyproline II (pPII) and β-strand conformations.[47] This observation suggests that only at high pH*, the low- and high-wavenumber groups of amide I′ bands represent predominantly peptide fibrils and monomers. At low pH*, the dispersion of amide I′ extends into the region above 1650 cm^{-1}. We will return to this conclusion below when we discuss time-resolved IR experiments.

Since all our data indicate that the deprotonation of the imidazole side chain of GHG is the trigger for GHG self-assembly and gelation, it makes sense to relate the amide I′ intensities to the concentration of this species. The latter has been estimated above with a simple titration model augmented by considering the ionic strength dependence of the pK value. We now relate the calculated $[\mathrm{GHG}]_{\mathrm{deprot}}$ values to the amide I′ compositions. Figure 5 displays the combined fractional integrated intensities of AI_1 and AI_2 which are both indicators of peptide self-assembly into ordered structures as a function of $[\mathrm{GHG}]_{\mathrm{deprot}}$. As expected from the abovementioned analysis of the IR spectra, only the respective intensities obtained from the 300 mM data set exhibit a monotonic behavior in that the fractional intensity increases nearly linearly with $[\mathrm{GHG}]_{\mathrm{deprot}}$ before plateauing above 100 mM. The respective fractional intensity of AI_1 which is also plotted in Figure 5 shows a similar although more sigmoidal behavior. At low concentrations of deprotonated GHG, AI_1 gains intensity at the expense of AI_4, as already suggested above. Above 80 mM, the growth of AI_1 coincides with an intensity decrease of AI_2 (cf. Figure 4). These data indicate that the number of peptides integrated in fibrils increases with $[\mathrm{GHG}]_{\mathrm{deprot}}$ until it reaches saturation close to the midpoint of the corresponding titration curve (Figure 2).

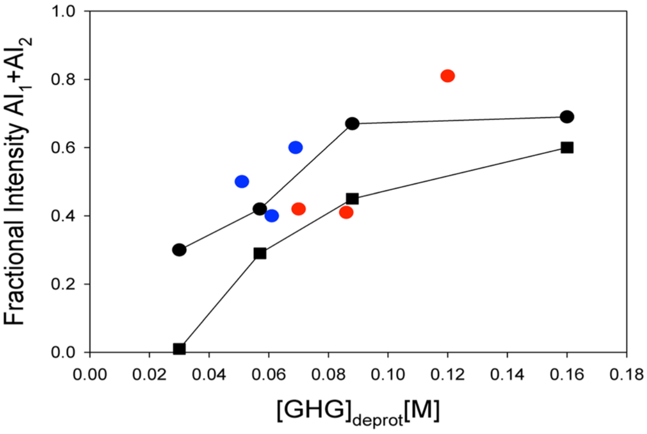

Figure 5. Combined fractional integrated intensities of the AI_1 and AI_2 plot as a function of the concentration of deprotonated GHG as derived from the amide I′ band profile of the GHG gels obtained with samples of 75 mM (red circles), 175 mM (blue circles), and 300 mM GHG (black circles). The integrated fractional intensities of AI_1 as obtained from the spectra of the 300 mM GHG sample are depicted as black squares. The solid lines in the figure solely connect the data points obtained from the spectra of the 300 mM sample.

As already indicated in Figure 4, the combined fractional AI_1 and AI_2 intensities obtained from the spectra of the 75 and 175 mM samples are more scattered and thus indicate a less monotonic behavior, but a general trend indicative of increasing self-assembly with increasing $[\mathrm{GHG}]_{\mathrm{deprot}}$ can be discerned from the data. One could therefore hypothesize that the scattering at low peptide concentrations may be indicative of a competition between fibril self-assembly into ordered fibrils and the formation of more disordered aggregates. Only at high peptide concentrations does the former dominate over the latter so that the respective amide I′ intensities display a clear monotonic behavior. Altogether, our data indicate that some self-assembly of GHG occurs even at 30 mM of deprotonated GHG. However, the formation of ordered fibrils indicated by AI_1 requires that $[\mathrm{GHG}]_{\mathrm{deprot}}$ exceeds a critical concentration of ca. 50−60 mM.

VCD Spectroscopy. VCD spectroscopy is a more recent addition to the toolbox by means of which one investigates supramolecular structures such as (amyloid) fibrils of peptides and proteins. Generally, the amide I modes of the underlying β-sheet structure exhibit only weak rotational strength since their chirality is not very pronounced.[46,48] An ideal rippled antiparallel β-sheet is built of unit cells with a C_{2h}-symmetry and exhibits an inversion center which makes it achiral. However, long fibrils of mostly achiral strands are frequently helically twisted which can induce an enormous enhancement of the rotational strength of amide I modes. This has been observed for amyloid fibrils of unfolded lysozyme[49] and insulin[50,51] and the fibrils of short oligopeptides[52,53] and L-alanine crystals.[56] Collectively, these results show that the observed VCD enhancement can be used as an indicator of the formation of ordered protein, peptide, and even amino acid fibrils with intrinsic chirality. Thus, its applicability goes beyond the normal use of IR spectra of β-sheets which allows the identification of β-sheets but does not distinguish between short sheets and long chiral fibrils. As shown by Farrell at al., VCD enhancement can occur even in non β-sheet fibrils formed by, for example, GAG in water/ethanol.[24]

Figure 6 shows the VCD spectra of 75, 175, and 300 mM GHG taken in the amide I′ region at the highest pH* investigated. We determined the influence of circular birefringence on these spectra by measuring them at the three different orientations described above.[40,54] Spectra taken with 75 and 300 mM GHG show a limited dependence on sample orientation, but the more pronounced signal observed for the R3 rotation of the latter should be noted. The corresponding amide I′ profiles can be described as positive couplets with the negative maxima close to the AI_1 position and the positive ones shifted to the red. As observed for other fibrils, the rotational strengths exceed that of monomeric GHG by nearly 2 orders of magnitude.[23] As indicated above, this enhancement might be attributed to some type of chirality, which in the case of a traditional β-sheet structure would be helically twisting.[52,55,56] Additionally, the anisotropy of the sample is likely to contribute to the VCD enhancement. Because of the large size of the fibrils they could not orient themselves along the optical axis of the spectrometer because of the limited size of optical path length (cf. Material and Methods).

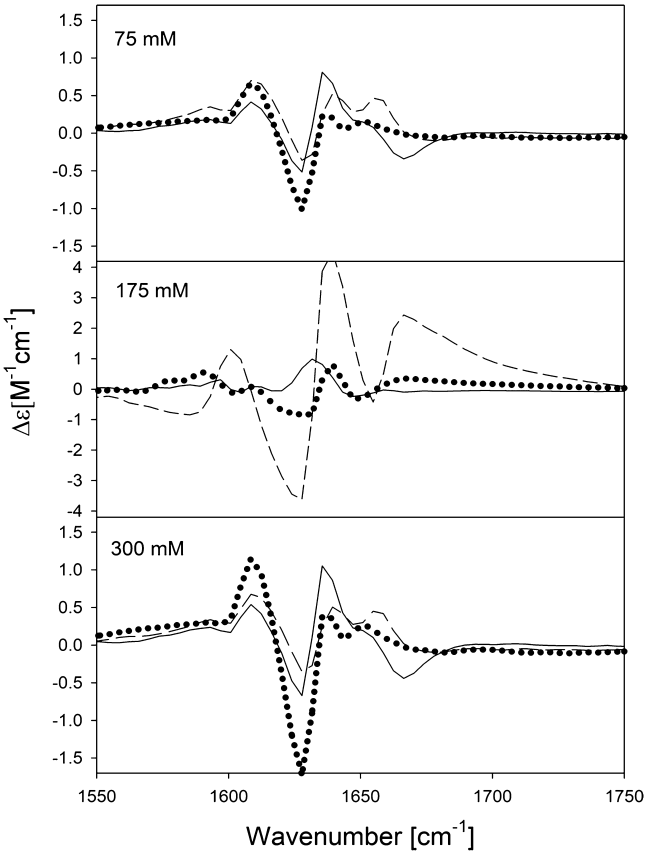

Figure 6. Amide I′ region of the VCD spectra of GHG measured pH* 7.38 (for 75 mM, upper panel), 6.84 (175 mM, middle panel), and 6.61 (300 mM, lower level). Spectra were taken with the orientation R1 (solid line), R2 (dashed line), and R3 (dotted line) used for the recording of the abovementioned IR spectra. The VCD spectra were scaled with the same factors used to unify the IR spectra in Figure 3 for the sake of quantitative consistency.

The couplet character of the amide I′ also reveals that AI_1 gains contributions from at least two excitonic transitions with opposite rotational strength. The 175 mM spectrum depends significantly more on the sample orientation which indicates some degree of anisotropy in the sample. This observation is fully consistent with the corresponding orientational dependence of the IR spectrum (vide supra, Figure 3). The different spectra even differ in terms of their sign sequence, but the most intense signal observed with R2 rotation is predominantly a negative couplet, similar to the ones observed for 75 and 300 mM. The pronounced VCD signal coincides with the very strong AI_1 band in the R2 IR spectrum (Figure 3). It should be noted that the 175 mM spectra are in qualitative agreement with spectra of a 175 mM sample reported by Hesser et al.[25].

Kinetics of Fibril Formation and Identification of the Fibrils′ Amide I′ Profile. As we have argued above, the amide I′ profiles of GHG fibrils extends well above 1650 cm^{-1}, which is somewhat uncharacteristic for β-sheets. The uniqueness of this observation requires additional investigation and discussion.

Figure 7 shows time-resolved FTIR spectra for 175 mM GHG at pH* 6.16, that is, just above the critical line in the gel formation phase diagram with an estimated concentration of deprotonated peptides of ca. 50 mM. Under these conditions, fibrillization kinetics are slow enough to be probed by ATR-IR. We used our Multifit program to decompose the spectra between 1300 and 1800 cm^{-1} after appropriate baseline subtraction. A large spectra region was chosen to ensure that we appropriately accounted for overlap with the amide I′ band. Figure S6 shows the four amide I′ bands and the intense COO^- antisymmetric stretching (COO^-_{as}) band at 1598 cm^{-1}

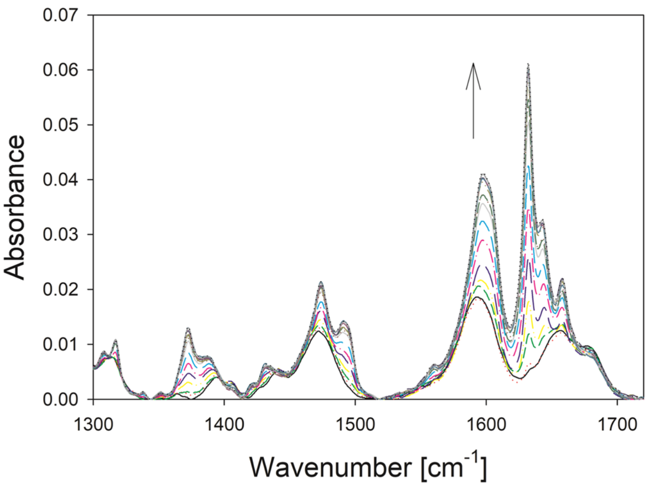

Figure 7. IR spectra of 175 mM GHG at pH* 6.19 measured as a function of time. The spectral development is indicated by an arrow. Spectra were taken after 38, 98, 204, 255, 312, 425, 476, 476, 525, 578, 660, 700, 756, and 1018 s with an ATR spectrometer.

derived from the last recorded spectrum (1018 s). Initially, we fit all spectra with the same number of bands, band positions, and half-widths. However, this only resulted in satisfactory fits for times longer than 300 s. Minor modifications were made to the model for the earlier recorded spectra. In each case, the amide I′ band profile was decomposed into the above-introduced set of four amide I′ bands.

Figure 8 shows plots of the integrated fractional intensities of AI_1, AI_3, AI_4, and COO^-_{as} bands. AI_2 is practically time-independent and is therefore not discussed in detail. The kinetic traces were fit with an empirical sigmoidal function given by

$$I(t) = I_0 + \left[\frac{\Delta I}{1 + \exp\left(\frac{-t - t_0}{\tau}\right)}\right] \qquad (4)$$

where I_0 is the intensity for $t \ll t_0$, ΔI is the maximal intensity change which can be positive or negative, t_0 is the time corresponding to the inflection point, and τ is a kinetic time constant that determines the slope of the sigmoidal curve. The solid lines in Figure 8 result from a nonlinear least squares regression performed in Sigma Plot. For our purpose t_0 and τ are the only relevant parameters to discuss, and the values are listed in Table 1.

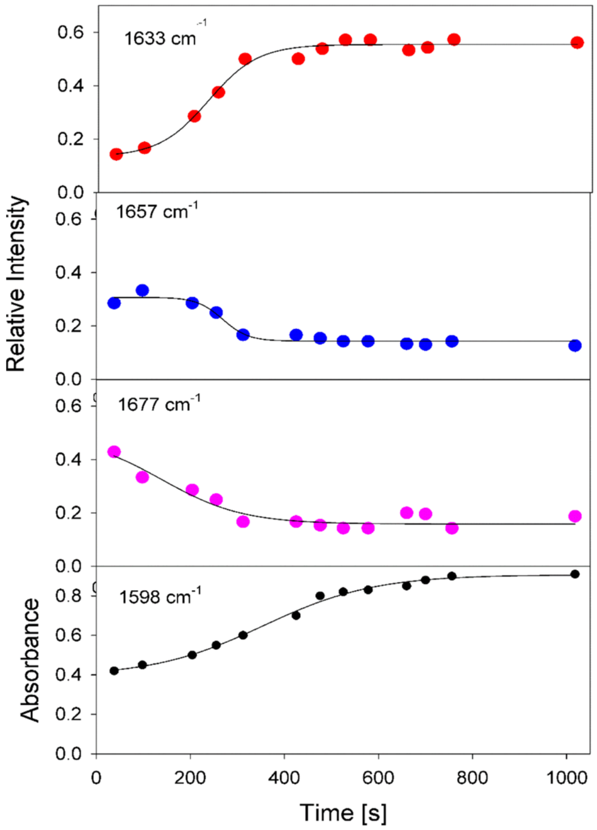

Figure 8. Fractional integrated intensities of amide I′ sub bands AI_1, AI_3, and AI_4 and the relative integrated intensity of the COO^- stretching band of 175 mM GHG at pH* 6.19 plotted as a function of time after incubation on the surface of an ATR IR spectrometer. The solid lines result from fits described in the text.

Table 1. Kinetic Parameters Obtained from the Fits in Figure 8

	τ [s]	t_0 [s]
COO^-_{as}	117 ± 13	355 ± 20
AI_1	52 ± 11	234 ± 11
AI_3	27 ± 9	268 ± 11
AI_4	85 ± 50	139 ± 113

Initially, one might be surprised by the increasing intensity of the COO^-_{as} band at 1598 cm^{-1} as a function of time. Normally, one would expect the intensity of this band to stay constant with time, since neither its oscillator strength nor its wavenumber position is expected to change drastically upon fibril formation and gelation. However, this observation becomes less of an issue if we consider the fact that the integrated intensities of amide I′ and of CH-deformation modes below 1500 cm^{-1} exhibit an increase in their respective intensities as well. This overall increase can be explained by the ATR technique, which only probes the first few micrometers of the millimeter-thick sample. Therefore, the increasing COO^-_{as} intensity is signifying that near the ATR crystal surface, there is a significant local increase in the number of deprotonated peptides. This corresponds to the presence of self-assembled peptide fibrils forming near the ATR crystal surface, which represent highly concentrated structures of peptides. In other words, by the end of the experiment, the ATR crystal is predominately sampling fibril structures, and thus, the amide I′ profile more closely resembles the spectrum of pure fibrils and possibly some incorporated monomers or short oligomers. While the fractional intensities of AI_3 and AI_4 decreased with time, they do not level off close to zero, which indicates that either contributes to the excitonic spectrum of the fibrils in this wavenumber region. Hence, we can conclude that the amide I′ profile of the GHG fibrils deviates from that of a canonical β-sheet.

Furthermore, the t_0 values for AI_1 and AI_3 are only slightly different, while the changes in AI_4 occurred on a faster time scale (Table 2). Since the intensity of AI_1 is not zero at the starting point of our experiment, a first fibril-forming burst phase must have occurred on a shorter time scale. The fast

Table 2. List of the Calculated Concentrations of Deprotonated GHG, Half Time of Gelation Kinetics, and Plateau Values of Rheological Parameters Obtained for the Indicated GHG Concentrations and pH* Values

	$[GHG]_{deprot}$ [M]	$t_{1/2}$ [min]	G' [Pa*10^5]	G'' [Pa*10^5]	tan δ
75 mM pH* 6.67	0.051	~200	0.003	0.0004	0.13
75 mM pH* 6.97	0.061	96	0.7	0.17	0.24
75 mM pH* 7.38	0.069	13	1.28	0.44	0.32
175 mM pH* 6.33	0.07	18	1.23	0.36	0.29
175 mM pH* 6.47	0.086	14	4	1.67	0.29
175 mM pH* 6.84	0.120	3	1.14	0.48	0.42
300 mM pH* 5.7	0.03	55	0.029	0.0064	0.22
300 mM pH* 5.92	0.057	22	0.76	0.19	0.25
300 mM pH* 6.13	0.088	7	2.3	0.79	0.34
300 mM pH* 6.61	0.160				

decay of AI_4 predominantly reflects the decrease in monomer concentrations during the initial phase of fibril formation. The different kinetic traces of AI_3 and AI_4 and the very similar t_0 values obtained for the kinetics of AI_1 and AI_3 confirm the notion that the spectra of initially formed GHG oligomers and fibrils contain contributions in the same spectral region above 1650 cm^{-1}. The larger half times of AI_1 and AI_3 reflect the time it takes for peptide fibrils to form and grow within the evanescent field. The rather large t_0 value of the kinetics probed by COO^{-}_{as} indicates that this process occurs on a slower time scale than the fibrillization process itself. Apparently, while peptide fibrils are forming, the overall amide I′ profile no longer changes, although its total integrated intensity still increases.

We conducted another measurement of IR kinetics for the 175 mM sample at pH* 6.38. An analysis of the amide I′ region in the spectrum taken at the end of the measurement revealed no substantial differences from the corresponding spectrum of the sample at the lower pH* value. This suggests that the amide I′ profile of the fibrillar state is independent of pH*. A comparison of the fractional amide I′ intensities obtained for the plateau spectra of our kinetic experiments with corresponding intensities observed with 300 mM GHG reveal very similar corresponding values. This observation suggests that the two 300 mM spectra measured at the two highest pH* values very much represent the spectra of the physically cross-linked fibril network with minimal interference from monomers. The similarities between the 300 mM spectra and the final spectra obtained at the end of our kinetic experiments are not surprising in view of the above-discussed accumulation of peptides in the sampling area of our ATR experiment.

Gelation Kinetics Measured for Different Points in the Gel Phase. Figure 9 shows the kinetics of gelation measured at the indicated pH* for different peptide concentrations using small amplitude oscillatory shear (SAOS). The pH* values are very close to those used for the abovementioned IR experiments. The plateau values of G'_{max} and G''_{max}, the corresponding tan δ values, the half time $t_{1/2}$ defined as $t(G' = G'_{max}/2)$ and the estimated concentrations of deprotonated peptides are all listed in Table 2. The data reveal a significant dependence of both the gelation rate and the final moduli on peptide concentration and final pH*. Figure S7 visualizes the concentration dependence of $t_{1/2}$, G', and G''. The depicted data reveal a rather complex picture. For a peptide concentration of 75 mM, the half time decreases linearly over a $[GHG]_{deprot}$ interval of only 20 mM. Concomitantly, the storage modulus increases from a very moderate value of 300 Pa to a very large value of $1.28 \cdot 10^5$ Pa. In contrast, the half times observed with 175 and 300 mM samples are all shorter and decrease much less over a much broader range of concentrations. The gelation kinetics of the 300 mM samples are much faster at the lowest pH* investigated than the corresponding kinetics of the 75 mM sample, even though the corresponding $[GHG]_{deprot}$ value is much lower. The concentration dependencies of G' and G'' for the 175 and 300 mM samples are also significantly less pronounced than the ones for the 75 mM samples. In fact, the 175 and 300 mM data overlap nicely and seem to be consistent with each other, while the lowest pH* 75 mM sample is clearly distinct. One possible hypothesis is that low $[GHG]_{deprot}$ leads to the formation of few nuclei that grow to form very porous networks, that is, low moduli. As pH* increases, $[GHG]_{deprot}$ increases, leading to more nuclei and a network with less porosity and thus to a higher modulus.

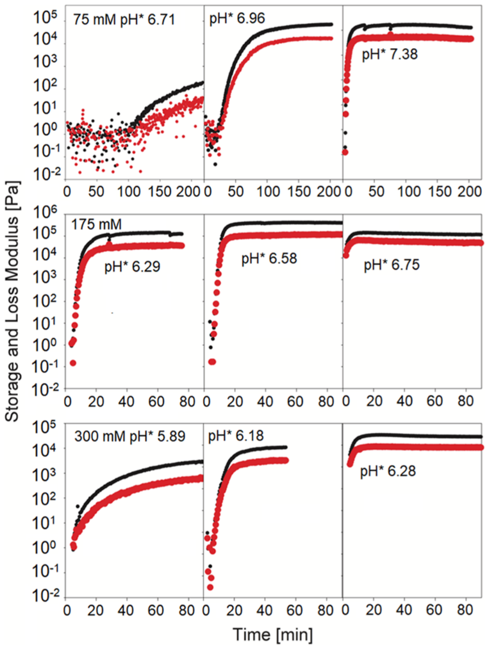

Figure 9. Gelation kinetics of GHG in water probing the time-dependent storage and loss modulus at the indicated pH* and peptide concentrations.

The concentration dependence of G' and G'' suggest an optimum concentration of deprotonated GHG close to 90 mM where the storage modulus is in the 10^5 regime. As observed for GAG in water ethanol, the two moduli do not increase monotonically with peptide concentration as other peptides generally do.[26,28] This observation is indicative of the importance of crystal growth kinetics in the final modulus. The crystal growth kinetics are expected to be a complicated function of pH and total dissolved peptide concentration. For example, too high of a peptide concentration (i.e., $[GHG]_{deprot}$) will lead to fast fibril kinetics and possibly favor bulk precipitation over fibril formation. A comparison of the above mentioned fibrillization kinetics with the time scale of gel formation reveals that the 300 mM kinetics is faster than the 175 mM one in both cases (cf. the t_0 values in Table 1 with the $t_{1/2}$ values in Table 2). The kinetics at 300 mM lead to a lower modulus, which suggests that the network is more porous. This argument is supported by the microscopy images presented below. Unfortunately, the uncertainty of the effective peptide concentration for the IR kinetics in Figure 8 precludes a more quantitative comparison of fibrillization and gelation kinetics.

Images of Gel Phases at Different Points of the Gel Phase. Figure 10 shows microscopic images of gels formed with peptide concentrations of 75, 175, and 300 mM at the highest pH* value investigated (vide supra). For the 75 mM sample, the image of the fibrils reveals an inhomogeneous gel phase which stresses the notion that a low concentration of deprotonated GHG leads to the formation of few nuclei and denser crystalline morphologies that do not produce a full sample spanning network. The situation is quite different for 175 mM GHG, where a homogeneous distribution of long fibril haystacks forms a sample spanning network. The images are fully consistent with the very high G' values revealed by

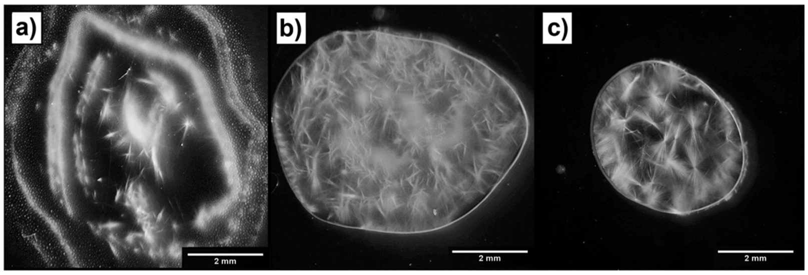

Figure 10. Microscopic images of gel samples with the following GHG concentrations and pH*: (a) 75 mM, pH* 7.0, (b) 175 mM, pH* 6.6, and (c) 300 mM, pH* 6.2.

rheology and the higher fraction of fibrils inferred from the IR spectra. The 300 mM sample image shows a more pronounced orientation of haystacks and denser fibril bundles (as seen around the periphery of the drop) compared to the 175 mM sample image. The reduced overlap of bundles at 300 mM is directly correlated to the lower modulus. Thus, the images reveal a picture similar to what we observed for GAG in water−ethanol mixtures, namely, the existence of an optimal peptide concentration where the number of fibrils is sufficiently large and homogeneously distributed to form a dense sample spanning network.[1] Below or above this concentration, the network is less homogeneous, leading to reduced gel strength. Recently, we explained a similar observation for GAG in water−ethanol; this fast liquid-peptide demixing due to fast network formation occurs at high peptide concentrations, which leads to the formation of colloid-like clusters of peptide fibrils and thus to the observed inhomogeneity.[28] In agreement with our reasoning, Draper and Adams emphasized in a recent review article that gelators might get trapped in what they called a kinetically driven assembly because the rate of fibrillization and gelation exceeds the rate of mixing.[4]

■ CONCLUSIONS

The spectroscopic, rheological, and microscopical investigation of the gel phase of GHG formed above pH* 5.5 reveals that the formed gel cannot be described in conventional categories. While the IR spectrum of the gel phase exhibits some characteristics of β-sheet formation, substantial intensities in the spectral region above 1650 cm^{-1} suggest that the secondary structure of formed fibrils differs from canonical β-sheets. This is coincidentally like the spectroscopic properties of GAG gels formed in water−ethanol, which also depart significantly from β-sheet characteristics. An analysis of the pH* dependence of gel spectra at three different peptide concentrations reveals a monotonic increase in fibril formation with an increasing concentration of deprotonated GHG at high (300 mM) peptide concentrations and a competition between fibril formation and the self-assembly in unordered aggregates at lower concentrations (75 and 175 mM). The critical concentration of deprotonated GHG required for the onset of the self-assembly process lies between 50 and 60 mM.

Rheology suggests an optimal concentration of deprotonated GHG that induces an isotropic homogeneous gel phase with a considerable modulus above 10^5 Pa. Overall, the rheological data suggest that peptide concentration and pH* can be used to tune the gel modulus over several orders of magnitude, which is important for applications such as drug delivery. The decrease in the half time of GHG gelation with increasing concentration of deprotonated GHG is very pronounced at the lowest peptide concentration investigated (i.e., 75 mM) and more modest at 175 and 300 mM (cf. Figure S7). These observations are consistent with the microscopic images in Figure 10 which reveal rather different sizes and modes of fibril organization for the 75 mM and the 175/300 mM samples, respectively. For the former, the images reveal several short unconnected haystack spots and a rather inhomogeneous organization of rather long fibrils at high pH*.[2] At higher concentrations, the haystacks are composed of long interpenetrating fibrils with significantly less porosity, even at the lowest pH* investigated.

There are several important issues regarding GHG gels that have not been addressed in this study. First of all, we do not yet fully understand the internal structure of the fibrils. Our currently in-progress analysis of wide-angle X-ray scattering data is aimed at obtaining a crystal structure which we could use to calculate amide I profiles which could be compared with experimental ones reported in this paper. Obtaining the internal structure of fibrils will allow us to decide whether self-assembly is predominantly promoted by hydrogen bonding between the imidazole nitrogens and peptide groups or by $\pi-\pi$ stacking of imidazole rings. Second, we plan to investigate in detail the thermal stability of the gel phase and its reversibility after annealing. Third, we will explore the stability of the gel via dilution and temperature effects. The outcome of it will determine the usefulness of GHG gels in relevant biomedical applications.

■ ASSOCIATED CONTENT

SI Supporting Information

The Supporting Information is available free of charge at https://pubs.acs.org/doi/10.1021/acs.langmuir.1c00382.

> Information about sample preparation, calculated titration curves for different total peptide (GHG) concentrations, original IR spectra of GHG gels obtained at different pH values with different peptide concentrations, spectral decomposition of the IR spectrum of a GHG gel, IR spectra of GHG taken with different sample orientations, spectral decomposition of an IR spectrum of a GHG gel measured with an ATR setup, peptide concentration dependence of sheet formation kinetics, and peptide concentration dependence of rheological moduli of GHG gels (PDF)

■ AUTHOR INFORMATION

Corresponding Authors

Nicolas J. Alvarez − *Department of Chemical and Biological Engineering, Drexel University, Philadelphia, Pennsylvania 19104, United States*; Email: nja49@drexel.edu

Reinhard Schweitzer-Stenner − *Department of Chemistry, Drexel University, Philadelphia, Pennsylvania 19104, United States;* orcid.org/0000-0001-5616-0722; Phone: 215-895-2268; Email: rs344@drexel.edu

Authors

Morgan Hesser − *Department of Chemistry, Drexel University, Philadelphia, Pennsylvania 19104, United States*

Lavenia J. Thursch − *Department of Chemical and Biological Engineering, Drexel University, Philadelphia, Pennsylvania 19104, United States*

Todd R. Lewis − *Department of Chemical and Biological Engineering, Drexel University, Philadelphia, Pennsylvania 19104, United States*

Thamires A. Lima − *Department of Chemical and Biological Engineering, Drexel University, Philadelphia, Pennsylvania 19104, United States;* orcid.org/0000-0003-2330-8318

Complete contact information is available at: https://pubs.acs.org/10.1021/acs.langmuir.1c00382

Notes

The authors declare no competing financial interest.

■ ACKNOWLEDGMENTS

Research reported in this paper was supported by a grant from the National Science Foundation to R.S.S. and N.J.A. (DMR-170770) and an REU-supplement for the support of M.H. (DMR-1915781). The Undergraduate research Co-op internship (cooperative education) of M.H. was further supported in part by a grant from the Steinbright Career Development Center of Drexel University.

■ REFERENCES

(1) De Leon Rodriguez, L. M.; Hemar, Y.; Cornish, J.; Brimble, M. A. Structure-mechanical property correlations of hydrogel forming β-sheet peptides. *Chem. Soc. Rev.* **2016**, *45*, 4797−4824.

(2) Seow, W. Y.; Hauser, C. A. E. Short to Ultrashort Peptide Hydrogels for Biomedical Uses. *Mater. Today* **2014**, *17*, 381−388.

(3) Adler-Abramovich, L.; Gazit, E. The Physical Properties of Supramolecular Peptide Assemblies: From Building Block Association to Technological Applications. *Chem. Soc. Rev.* **2014**, *43*, 6881−6893.

(4) Draper, E. R.; Adams, D. J. Low-Molecular-Weight Gels: The State of the Art. *Chem* **2017**, *3*, 390−410.

(5) Rajagopal, K.; Schneider, J. P. Self-Assembling Peptides and Proteins for Nanotechnological Applications. *Curr. Opin. Struct. Biol.* **2004**, *14*, 480−486.

(6) Hirst, A. R.; Escuder, B.; Miravet, J. F.; Smith, D. K. High-Tech Applications of Self-Assembling Supramolecular Nanostructured Gel-Phase Materials: From Regenerative Medicine to Electronic Devices. *Angew. Chem., Int. Ed.* **2008**, *47*, 8002−8018.

(7) Hamley, I. W. Peptide Fibrillization. *Angew. Chem., Int. Ed.* **2007**, *46*, 8128−8147.

(8) Nguyen, H. D.; Hall, C. K. Kinetics of Fibril Formation by Polyalanine Peptides. *J. Biol. Chem.* **2005**, *280*, 9074−9082.

(9) Measey, T. J.; Schweitzer-Stenner, R. Aggregation of the Amphipathic Peptides (AAKA)ninto Antiparallel β-Sheets. *J. Am. Chem. Soc.* **2006**, *128*, 13324−13325.

(10) Yokoi, H.; Kinoshita, T.; Zhang, S. Dynamic Reassembly of Peptide RADA16 Nanofiber Scaffold. *Proc. Natl. Acad. Sci. U.S.A.* **2005**, *102*, 8414−8419.

(11) Zhao, Y.; Yokoi, H.; Tanaka, M.; Kinoshita, T.; Tan, T. Self-Assembled PH-Responsive Hydrogels Composed of the RATEA16 Peptide. *Biomacromolecules* **2008**, *9*, 1511−1518.

(12) Wang, J.; Tang, F.; Li, F.; Lin, J.; Zhang, Y.; Du, L.; Zhao, X. The Amphiphilic Self-Assembling Peptide EAK16-I as a Potential Hydrophobic Drug Carrier. *J. Nanomater.* **2008**, *2008*, 1−8.

(13) Gazit, E. Self Assembly of Short Aromatic Peptides into Amyloid Fibrils and Related Nanostructures. *Prion* **2007**, *1*, 32−35.

(14) Orbach, R.; Adler-Abramovich, L.; Zigerson, S.; Mironi-Harpaz, I.; Seliktar, D.; Gazit, E. Self-Assembled Fmoc-Peptides as a Platform for the Formation of Nanostructures and Hydrogels. *Biomacromolecules* **2009**, *10*, 2646−2651.

(15) Ghosh, M.; Halperin-Sternfeld, M.; Grinberg, I.; Adler-Abramovich, L. Injectable Alginate-Peptide Composite Hydrogel as a Scaffold for Bone Tissue Regeneration. *Nanomaterials* **2019**, *9*, 497.

(16) Ghosh, M.; Halperin-Sternfeld, M.; Grigoriants, I.; Lee, J.; Nam, K. T.; Adler-Abramovich, L. Arginine-Presenting Peptide Hydrogels Decorated with Hydroxyapatite as Biomimetic Scaffolds for Bone Regeneration. *Biomacromolecules* **2017**, *18*, 3541−3550.

(17) Fleming, S.; Ulijn, R. V. Design of Nanostructures Based on Aromatic Peptide Amphiphiles. *Chem. Soc. Rev.* **2014**, *43*, 8150−8177.

(18) Ulijn, R. V. Molecular Self-Assembly: Best of Both Worlds. *Nat. Nanotechnol.* **2015**, *10*, 295−296.

(19) Smith, A. M.; Williams, R. J.; Tang, C.; Coppo, P.; Collins, R. F.; Turner, M. L.; Saiani, A.; Ulijn, R. V. Fmoc-Diphenylalanine Self Assembles to a Hydrogel via a Novel Architecture Based on π-π Interlocked β-Sheets. *Adv. Mater.* **2008**, *20*, 37−41.

(20) Frederix, P. W. J. M.; Scott, G. G.; Abul-Haija, Y. M.; Kalafatovic, D.; Pappas, C. G.; Javid, N.; Hunt, N. T.; Ulijn, R. V.; Tuttle, T. Exploring the Sequence Space for (Tri-)Peptide Self-Assembly to Design and Discover New Hydrogels. *Nat. Chem.* **2015**, *7*, 30−37.

(21) Frederix, P. W. J. M.; Ulijn, R. V.; Hunt, N. T.; Tuttle, T. Virtual Screening for Dipeptide Aggregation: Toward Predictive Tools for Peptide Self-Assembly. *J. Phys. Chem. Lett.* **2011**, *2*, 2380−2384.

(22) Milorey, B.; Farrell, S.; Toal, S. E.; Schweitzer-Stenner, R. Demixing of Water and Ethanol Causes Conformational Redistribution and Gelation of the Cationic GAG Tripeptide. *Chem. Commun.* **2015**, *51*, 16498−16501.

(23) DiGuiseppi, D.; Schweitzer-Stenner, R. Probing Conformational Propensities of Histidine in Different Protonation States of the Unblocked Glycyl-Histidyl-Glycine Peptide by Vibrational and NMR Spectroscopy. *J. Raman Spectrosc.* **2016**, *47*, 1063−1072.

(24) Farrell, S.; DiGuiseppi, D.; Alvarez, N.; Schweitzer-Stenner, R. The Interplay of Aggregation, Fibrillization and Gelation of an Unexpected Low Molecular Weight Gelator: Glycylalanylglycine in Ethanol/Water. *Soft Matter* **2016**, *12*, 6096−6110.

(25) Hesser, M.; Thursch, L.; Lewis, T.; DiGuiseppi, D.; Alvarez, N. J.; Schweitzer-Stenner, R. The Tripeptide GHG as an Unexpected Hydrogelator Triggered by Imidazole Deprotonation. *Soft Matter* **2020**, *16*, 4110−4114.

(26) Thursch, L. J.; DiGuiseppi, D.; Lewis, T. R.; Schweitzer-Stenner, R.; Alvarez, N. J. Exploring the Gel Phase of Cationic Glycylalanylglycine in Ethanol/Water. I. Rheology and Microscopy Studies. *J. Colloid Interface Sci.* **2020**, *564*, 499−509.

(27) DiGuiseppi, D.; Thursch, L.; Alvarez, N. J.; Schweitzer-Stenner, R. Exploring the Thermal Reversibility and Tunability of a Low Molecular Weight Gelator Using Vibrational and Electronic Spectroscopy and Rheology. *Soft Matter* **2019**, *15*, 3418−3431.

(28) DiGuiseppi, D. M.; Thursch, L.; Alvarez, N. J.; Schweitzer-Stenner, R. Exploring the Gel Phase of Cationic Glycylalanylglycine in Ethanol/Water. II. Spectroscopic, Kinetic and Thermodynamic Studies. *J. Colloid Interface Sci.* **2020**, *573*, 123−134.

(29) Li, S.; Hong, M. Protonation, Tautomerization, and Rotameric Structure of Histidine: A Comprehensive Study by Magic-Angle-Spinning Solid-State NMR. *J. Am. Chem. Soc.* **2011**, *133*, 1534−1544.

(30) Movellan, K. T.; Wegstroth, M.; Overkamp, K.; Leonov, A.; Becker, S.; Andreas, L. B. Imidazole-Imidazole Hydrogen Bonding in the PH Sensing Histidine Sidechains of Influenza A M2. *J. Am. Chem. Soc.* **2020**, *142*, 2704−2708.

(31) Moyer, T. J.; Finbloom, J. A.; Chen, F.; Toft, D. J.; Cryns, V. L.; Stupp, S. I. PH and Amphiphilic Structure Direct Supramolecular Behavior in Biofunctional Assemblies. *J. Am. Chem. Soc.* **2014**, *136*, 14746−14752.

(32) van Bommel, K. J. C.; van der Pol, C.; Muizebelt, I.; Friggeri, A.; Heeres, A.; Meetsma, A.; Feringa, B. L.; van Esch, J. Responsive Cyclohexane-Based Low-Molecular-Weight Hydrogelators with Modular Architecture. *Angew. Chem.* **2004**, *116*, 1695−1699.

(33) Veerman, C.; Rajagopal, K.; Palla, C. S.; Pochan, D. J.; Schneider, J. P.; Furst, E. M. Gelation Kinetics of *β*-Hairpin Peptide Hydrogel Networks. *Macromolecules* **2006**, *39*, 6608−6614.

(34) Ozbas, B.; Kretsinger, J.; Rajagopal, K.; Schneider, J. P.; Pochan, D. J. Salt-Triggered Peptide Folding and Consequent Self-Assembly into Hydrogels with Tunable Modulus. *Macromolecules* **2004**, *37*, 7331−7337.

(35) Ilawe, N. V.; Schweitzer-Stenner, R.; Diguiseppi, D.; Wong, B. M. Is a cross-*β*-sheet structure of low molecular weight peptides necessary for the formation of fibrils and peptide hydrogels? *Phys. Chem. Chem. Phys.* **2018**, *20*, 18158−18168.

(36) Glasoe, P. K.; Long, F. A. Use of Glass Electrodes to Measure Acidities in Deuterium Oxide1,2. *J. Phys. Chem.* **1960**, *64*, 188−190.

(37) Jentzen, W.; Unger, E.; Karvounis, G.; Shelnutt, J. A.; Dreybrodt, W.; Schweitzer-Stenner, R. Conformational Properties of Nickel(II) Octaethylporphyrin in Solution. 1. Resonance Excitation Profiles and Temperature Dependence of Structure-Sensitive Raman Lines. *J. Phys. Chem.* **1996**, *100*, 14184−14191.

(38) Wright, M. R. *An Introduction to Aqueous Electrolyte Solutions*; Wiley & Sons, Inc., 2007; Vol. 45.

(39) Schweitzer-Stenner, R.; Eker, F.; Huang, Q.; Griebenow, K. Dihedral Angles of Trialanine in D2O Determined by Combining FTIR and Polarized Visible Raman Spectroscopy. *J. Am. Chem. Soc.* **2001**, *123*, 9628−9633.

(40) Lombardi, R. A.; Nafie, L. A. Observation and Calculation of Vibrational Circular Birefringence: A New Form of Vibrational Optical Activity. *Chirality* **2009**, *21*, No. E277.

(41) Sidler, D.; Bleiziffer, P.; Riniker, S. Beyond the Rosenfeld Equation: Computation of Vibrational Circular Dichroism Spectra for Anisotropic Solutions. *J. Chem. Theory Comput.* **2019**, *15*, 2492−2503.

(42) Lee, C.; Cho, M. Local Amide I Mode Frequencies and Coupling Constants in Multiple-Stranded Antiparallel *β*-Sheet Polypeptides. *J. Phys. Chem. B* **2004**, *108*, 20397−20407.

(43) Karjalainen, E.-L.; Ravi, H. K.; Barth, A. Simulation of the Amide I Absorption of Stacked *β*-Sheets. *J. Phys. Chem. B* **2011**, *115*, 749−757.

(44) Schweitzer-Stenner, R. Simulated IR, Isotropic and Anisotropic Raman, and Vibrational Circular Dichroism Amide I Band Profiles of Stacked *β*-Sheets. *J. Phys. Chem. B* **2012**, *116*, 4141−4153.

(45) Bandekar, J.; Krimm, S. Normal mode spectrum of the parallel-chain ?-sheet. *Biopolymers* **1988**, *27*, 909−921.

(46) Bour, P.; Keiderling, T. A. Structure, spectra and the effects of twisting of *β*-sheet peptides. A density functional theory study. *J. Mol. Struct.: THEOCHEM* **2004**, *675*, 95−105.

(47) Hagarman, A.; Measey, T. J.; Mathieu, D.; Schwalbe, H.; Schweitzer-Stenner, R. Intrinsic Propensities of Amino Acid Residues in GxG Peptides Inferred from Amide I′ Band Profiles and NMR Scalar Coupling Constants. *J. Am. Chem. Soc.* **2010**, *132*, 540−551.

(48) Measey, T.; Schweitzer-Stenner, R. The Conformations Adopted by the Octamer Peptide (AAKA)2 in Aqueous Solution Probed by FTIR and Polarized Raman Spectroscopy. *J. Raman Spectrosc.* **2006**, *37*, 248−254.

(49) Ma, S.; Cao, X.; Mak, M.; Sadik, A.; Walkner, C.; Freedman, T. B.; Lednev, I. K.; Dukor, R. K.; Nafie, L. A. Vibrational Circular Dichroism Shows Unusual Sensitivity to Protein Fibril Formation and Development in Solution. *J. Am. Chem. Soc.* **2007**, *129*, 12364−12365.

(50) Kurouski, D.; Lombardi, R. A.; Dukor, R. K.; Lednev, I. K.; Nafie, L. A. Direct Observation and PH Control of Reversed Supramolecular Chirality in Insulin Fibrils by Vibrational Circular Dichroism. *Chem. Commun.* **2010**, *46*, 7154−7156.

(51) Kurouski, D.; Dukor, R. K.; Lu, X.; Nafie, L. A.; Lednev, I. K. Normal and Reversed Supramolecular Chirality of Insulin Fibrils Probed by Vibrational Circular Dichroism at the Protofilament Level of Fibril Structure. *Biophys. J.* **2012**, *103*, 522−531.

(52) Measey, T. J.; Schweitzer-Stenner, R. Vibrational Circular Dichroism as a Probe of Fibrillogenesis: The Origin of the Anomalous Intensity Enhancement of Amyloid-like Fibrils. *J. Am. Chem. Soc.* **2011**, *133*, 1066−1076.

(53) Measey, T. J.; Smith, K. B.; Decatur, S. M.; Zhao, L.; Yang, G.; Schweitzer-Stenner, R. Self-Aggregation of a Polyalanine Octamer Promoted by Its C-Terminal Tyrosine and Probed by a Strongly Enhanced Vibrational Circular Dichroism Signal. *J. Am. Chem. Soc.* **2009**, *131*, 18218−18219.

(54) Wolffs, M.; George, S. J.; Tomović, Ž.; Meskers, S. C. J.; Schenning, A. P. H. J.; Meijer, E. W. Macroscopic Origin of Circular Dichroism Effects by Alignment of Self-Assembled Fibers in Solution. *Angew. Chem., Int. Ed.* **2007**, *46*, 8203−8205.

(55) Kessler, J.; Keiderling, T. A.; Bouř, P. Arrangement of Fibril Side Chains Studied by Molecular Dynamics and Simulated Infrared and Vibrational Circular Dichroism Spectra. *J. Phys. Chem. B* **2014**, *118*, 6937−6945.

(56) Jähnigen, S.; Scherrer, A.; Vuilleumier, R.; Sebastiani, D. Chiral Crystal Packing Induces Enhancement of Vibrational Circular Dichroism. *Angew. Chem., Int. Ed.* **2018**, *57*, 13344−13348.